Supersolid stacks in antidipolar Bose-Einstein condensates

K. Mukherjee ⬤, M. Nilsson Tengstrand, T. Arnone Cardinale ⬤, and S. M. Reimann ⬤

Mathematical Physics and NanoLund, LTH, Lund University, Box 118, 22100 Lund, Sweden

We theoretically investigate a supersolid structure taking the form of stacked, disk-shaped superfluid droplets connected via a dilute superfluid, in an antidipolar condensate. A phase diagram is determined for varying the particle number and scattering length, identifying the regions of a regular dipolar superfluid, supersolid stacks, and isolated stacked disk-shaped droplets in an experimentally realizable trapping potential. The collective Bogoliubov excitation spectrum across the superfluid-supersolid phase transition is studied, and the transition point is found to be associated with the breaking of the degeneracy of the two lowest-lying modes. The dynamical generation of the supersolid stacks is also investigated by ramping down the scattering length across the phase transition. Moreover, we have studied the impact of vortex-line penetration on the phase transition. We have found that the presence of a vortex line causes the supersolid region to move towards weaker contact interactions. Our detailed numerical simulations highlight that an antidipolar condensate can create such supersolid stacks within an experimentally reachable parameter regime.

I. INTRODUCTION

Dipolar Bose-Einstein condensates (BECs) offer an intriguing platform [1–5] to study the supersolid state of matter [6–13], displaying both diagonal and off-diagonal long-range order [14–20]. In a supersolid, translational symmetry is spontaneously broken, leading to density modulations while partially maintaining superfluid (SF) properties. The concept was originally introduced and debated over an extensive period of time in the context of ^{4}He [20–24]; however, only recently ultracold atoms have emerged as a viable alternative setup [25–31]. Experiments involving highly magnetic dysprosium [32–35] and erbium atoms [36,37] uncovered the emergence of supersolidity in (quasi)one [7,35,37,38] as well as two spatial dimensions [39–41]. The underlying mechanism is attributed to the interplay between interparticle interactions and quantum fluctuations [42–44], a mechanism similar to the one seen in binary Bose gases forming droplets [45–47] which also have been realized experimentally [48–50]. Owing to the unique and fascinating properties of dipolar droplets and supersolids, there has been a recent surge in research focused on understanding these systems [13,44,51–73], including the exploration of out-of-equilibrium dynamics [38,74–76], vortices [77–79], and extensions to dipolar mixtures [80–85].

The bulk of current and recent work set focus on dipole-dipole interactions (DDIs) under a fixed magnetic field, oriented along a particular direction, say, the z axis. However,

by rotating the polarizing magnetic field (a technique also demonstrated in experiments [86]) it is possible to manipulate the dipole-dipole interaction [87,88]. A time-averaged DDI can be utilized when the rotation frequency exceeds the trap frequencies but is still smaller than the Larmor frequency. The magnitude and polarity of this DDI are determined by the angle between the dipole and the z axis [89]. By adjusting the tilt angle, the effective interaction can be modulated from dipolar to antidipolar regimes where the dipolar interaction is reversed. In this case, head-to-tail antidipoles repel, while side-by-side antidipoles attract, which is just opposite to the behavior observed in the ordinary dipolar regime. In a single trapped antidipolar condensate, stacks of disklike droplets may form that can even be supersolid when the disks connect by a dilute superfluid. These structures are quite different from the usual linear arrays of elongated filaments found in conventional dipolar condensates, as mentioned early on in the Ph.D. work of Wenzel [90]. Stacked droplets (SDs) or supersolids however have, to the best of our knowledge, not yet gained much attention, despite the in principle realistic experimental scenario, and the many interesting future prospects concerning for example studies of vorticity in such systems. Similar stacked supersolid structures were previously only discussed for a different setting of dipolar and nondipolar mixtures [91], where the immiscibility of the components stabilized the system. Other theoretical [68,92] or experimental studies [93,94] with focus on layered structures of dipolar gases required an optical lattice potential [92–94] or an electric dipole moment [68] for their fabrication. While Ref. [68] briefly addresses the observation of stacked droplet crystals in a doubly dipolar condensate with both electric and magnetic dipole moments, it is of interest to explore in detail the possibility of generating similar structures in a simpler system with only a single dipolar ingredient. Furthermore, it is vital to investigate the range of parameters where such droplet crystals exist in relation to

varying particle numbers and to explore their dynamical formation. Understanding these aspects is crucial for facilitating future experimental studies.

Here, we set focus on the antidipolar single-component condensates where, remarkably, the rather unique stack structures can arise exclusively from the combined effects of long-range and contact forces [90]. The layers can be completely isolated from each other, or be connected by a superfluid link, forming a different type of supersolid that we in the following refer to as a "supersolid stack" (SSS). We determine the ground-state phase diagram depicting the SF phase, SSS, and isolated SDs as a function of particle number and scattering length, with a fixed antidipolar length. After demarcating the explicit phase boundaries, we proceed to analyze the low-lying collective excitation spectra across the transition using a linear stability analysis based on the Bogoliubov–de Gennes (BdG) approach [12,95–99]. A crucial finding is that the degeneracy of the two lowest modes is broken at the transition point, serving as an indicator of the SF-SSS phase transition. Additionally, we provide evidence that the generation of layered structures can be achieved dynamically from a superfluid state by performing an interaction quench. Such a quenching technique for supersolid state generation is frequently used for regular dipolar condensates [6,7,41]. Quenching the interaction across the phase boundary results in density oscillations that we have found to be associated with patterns in the low-lying excitation spectra of the system. Finally, we investigate the impact of imposing a vortex line through the stacks. Our analysis reveals that a higher-charge vortex shifts the supersolid phase towards lower scattering lengths relative to the system without a vortex. Intriguingly, this suggests that the presence of a vortex affects the superfluid connection and reduces the density of the crystal structure.

The remainder of the paper is structured as follows. Section II describes the extended Gross-Pitaevskii (eGP) equation and the BdG approach. In Sec. III, we present the ground-state properties of an antidipolar condensate, delineating the phase diagram in Sec. III A, and describing the collective excitation properties in Sec. III B. The dynamical formation of a layered supersolid structure is addressed in Sec. IV A, and collective oscillations in Sec. IV B. The effect of a vortex line on supersolidity is discussed in Sec. V. We provide a summary of our findings, along with future perspectives, in Sec. VI. In Appendix A, we discuss the impact of a three-body loss term. Appendix B provides some details of our numerical simulations.

II. MODEL AND METHODS

A. Extended Gross-Pitaevskii equation

We consider a dipolar BEC (dBEC) composed of atoms with mass M and magnetic dipole moment μ_m. The dBEC is confined within a three-dimensional (3D) harmonic trapping potential of the form $V(\mathbf{r}) = M(\omega_x^2 x^2 + \omega_y^2 y^2 + \omega_z^2 z^2)/2$. For a schematic illustration of our setup, see Fig. 1. The atomic dipoles are aligned with a rotating uniform magnetic field $\mathbf{B}(t) = B\mathbf{e}(t)$, where $\mathbf{e}(t) = \cos\phi\mathbf{e}_z + \sin\phi[\cos(\Omega t)\mathbf{e}_x + \sin(\Omega t)\mathbf{e}_y]$ points out the
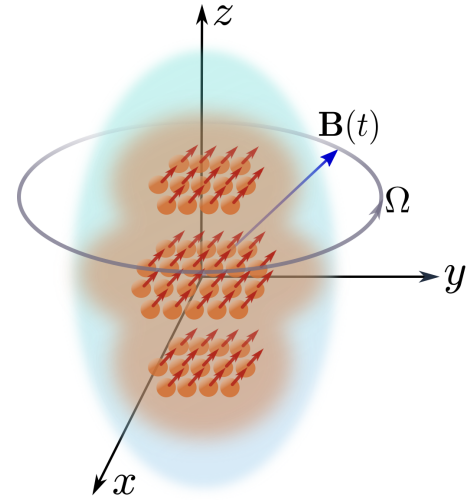

FIG. 1. Schematic illustration of the spontaneous formation of a layered structure in an antidipolar Bose-Einstein condensate confined in an elongated geometry along the z axis. The system is under the influence of a magnetic field rotating at a frequency Ω and an angle $\phi > 54.7°$. The rotation frequency is significantly larger than the trap frequency but smaller than the so-called Larmor frequency.

instantaneous direction of the magnetic field [88,89]. Here, $\mathbf{e}_x$, $\mathbf{e}_y$, and $\mathbf{e}_z$ are the unit vectors in the x, y, and z spatial directions, respectively, and Ω denotes the rotation frequency. Furthermore, it is assumed that the distances between the dipoles are much larger than the size of individual dipoles. Under such condition, the general expression of the DDI potential reads $U_{dd}^G(\mathbf{r}, t) = \frac{\mu_0 \mu_m^2}{4\pi}[\frac{1-3(\mathbf{e}(t)\cdot\hat{r})^2}{r^3}]$, where μ_0 corresponds to the permeability of vacuum. If the external magnetic field rapidly rotates at an angle ϕ relative to the z axis $\omega_i \ll \Omega \ll \omega_L = \mu B/\hbar$, where ω_L and ω_i ($i = x, y, z$) are the so-called Larmor frequency and trap frequencies, respectively, it becomes possible to perform a time-averaging process on the DDI over a complete rotation cycle of the polarizing magnetic field. Furthermore, since the rotation frequency of the magnetic field is significantly larger than the trap frequencies, the dynamical instabilities are strongly suppressed [88]. The time-averaged DDI is given by [87]

$$U_{dd}(\mathbf{r}) = \langle U_{dd}^G(\mathbf{r}, t)\rangle = \frac{\Omega}{2\pi}\int_0^{\frac{2\pi}{\Omega}} U_{dd}^G(\mathbf{r}, t)dt$$

$$= \frac{\mu_0\mu_m^2}{4\pi}\left(\frac{3\cos^2\phi - 1}{2}\right)\left(\frac{1 - 3\cos^2\theta}{|\mathbf{r}|^3}\right), \quad (1)$$

where θ denotes the angle between $\mathbf{r}$ and the z axis. The DDI is highly dependent upon the orientation of the constituent dipoles. The interaction vanishes entirely at the so-called magic angle, denoted by $\phi_m \approx 54.7°$. Specifically, for $\phi < \phi_m$, the preferred orientation of the dipoles is head to tail, while for $\phi > \phi_m$, an antidipolar configuration with a side-by-side arrangement of dipoles becomes energetically favorable. At zero temperature, the system is well described by the eGP

equation [36,42,43]

$$i\hbar\partial_t\psi(\mathbf{r},t) = \left[-\frac{\hbar^2}{2M}\nabla^2 + V(\mathbf{r}) + g|\psi(\mathbf{r},t)|^2 + \frac{3}{4\pi}g_{dd} \right.$$
$$\times \int d\mathbf{r}' \frac{1 - 3\cos^2\theta}{|\mathbf{r}-\mathbf{r}'|^3}|\psi(\mathbf{r}',t)|^2$$
$$\left. + \gamma(\epsilon_{dd})|\psi(\mathbf{r},t)|^3 \right]\psi(\mathbf{r},t). \quad (2)$$

Here, the short-range repulsive contact interaction, $g = 4\pi\hbar^2 a/M$, is determined by the s-wave scattering length a. The dipolar interaction coefficient is $g_{dd} = 4\pi\hbar^2 a_{dd}/M$ with $a_{dd} = \mu_0\mu_m^2 M(3\cos^2\phi - 1)/24\pi\hbar^2$ being the so-called dipolar length. The final term in Eq. (2) is given by the repulsive Lee-Huang-Yang correction with $\gamma(\epsilon_{dd}) = \frac{32}{3}g\sqrt{\frac{a^3}{\pi}}$ $(1 + \frac{3}{2}\epsilon_{dd}^2)$ [42,100,101], where the dimensionless parameter $\epsilon_{dd} = a_{dd}/a$ quantifies the relative strength of the DDI compared to the contact interaction. The solution of Eq. (2) is obtained by employing the split-step Crank-Nicolson method [102,103] in imaginary time to determine the initial ground state, and in real time to monitor the system's dynamics. The behavior of the system can be classified into different phases depending on the absolute value of the parameter ϵ_{dd}. When $|\epsilon_{dd}|$ is sufficiently small, the system exhibits a superfluid phase. However, for larger values of $|\epsilon_{dd}|$, the supersolid phase is favored within a specific range of values of $|\epsilon_{dd}|$. Beyond this range, the system transitions into the isolated droplet phase.

In the following, we consider a dBEC of ^{164}Dy atoms with a magnetic moment of $\mu_m = 9.93\mu_B$, where μ_B is the Bohr magneton. The system is examined in the maximally antidipolar regime, with $\phi = \pi/2$. This particular configuration leads to an overall factor of $-1/2$ in Eq. (1) compared to nonrotating dipoles corresponding to $\phi = 0°$. Consequently, the dipolar length becomes $a_{dd} = -65.5a_0$, where a_0 is the Bohr radius. The frequencies of the harmonic potential used in this paper are $\omega_x/(2\pi) = 100$ Hz, $\omega_y/(2\pi) = 100$ Hz, and $\omega_z/(2\pi) = 50$ Hz, resulting in an elongated geometry along the z axis. The aforementioned trapping frequencies and interaction strengths can be achieved in current experiments involving magnetic atoms [6,36,37,41,86,90].

B. BdG approach

In order to unveil the collective excitation spectrum of the system, we perform a Bogoliubov–de Gennes analysis [104,105]. To do so, we perturb the equilibrium solution ψ_0 using the following ansatz:

$$\psi(\mathbf{r},t) = \{\psi_0(\mathbf{r}) + \epsilon[u(\mathbf{r})e^{-i\Omega t} + v^*(\mathbf{r})e^{i\Omega t}]\}e^{-i\mu t/\hbar}. \quad (3)$$

The parameter ϵ represents a small-amplitude perturbation, while μ is the chemical potential. The eigenfrequencies and eigenfunctions, represented by Ω and (u, v^*), respectively, are the solutions of the eigenvalue problem resulting from the substitution of Eq. (3) into Eq. (2) with terms retained up to the first order in ϵ. Specifically,

$$\begin{pmatrix} H_s - \mu + X & X \\ -X & -(H_s - \mu + X) \end{pmatrix}\begin{pmatrix} u \\ v \end{pmatrix} = \hbar\Omega\begin{pmatrix} u \\ v \end{pmatrix}, \quad (4)$$

where $H_s = -\frac{\hbar^2}{2M}\nabla^2 + V(\mathbf{r})$ is the single-particle Hamiltonian, and the operator X is defined by its action on $q = u, v$ according to

$$Xq(\mathbf{r}) = \int d\mathbf{r}' U_{dd}(\mathbf{r} - \mathbf{r}')\psi_0^*(\mathbf{r}')\psi_0(\mathbf{r})q(\mathbf{r}')$$
$$+ g|\psi_0(\mathbf{r})|^2 q(\mathbf{r}) + \frac{3\gamma}{2}|\psi_0(\mathbf{r})|^3 q(\mathbf{r}). \quad (5)$$

Through the variable transformations $f = (u + v)/\sqrt{2}$ and $g = (u - v)/\sqrt{2}$, Eq. (4) can be reduced to two equations with only half the dimensions of the original ones. The resulting reduced equations are then solved by using standard diagonalization methods.

III. GROUND-STATE PROPERTIES

Our investigation focuses on exploring the ground-state properties of the antidipolar condensate, with the primary objective of identifying various density structures, determining their region of existence in a phase diagram, and mapping the underlying collective excitation properties during the phase transition. Furthermore, we explore the impact of the number of disks on the sharpness of the phase transition.

A. Identification of different phases

Figure 2 displays various ground-state density profiles featuring the unmodulated and modulated phases. For large scattering lengths where the contact interaction dominates the dipolar interaction, a typical superfluid density profile elongated along the z direction is formed, as shown in Fig. 2(a) for $N = 1.3 \times 10^5$ particles at $a = 110a_0$. As the relative strength of the dipolar interaction $|\varepsilon_{dd}|$ increases, side-by-side configurations become more favored, leading to their arrangement in the radial plane. However, the presence of a tight radial confinement breaks the condensate into multiple segments along the z direction as the configuration with lowest energy, resulting in the formation of stacked disks. Examples of modulated density structures for two different particle numbers are presented in Figs. 2(b) and 2(c), which demonstrate that the individual disks are connected by a dilute background density, substantiating a SSS phase.[1] Note that the number and distribution of disks along the z direction strongly depend on the total number of particles. For instance, a four-crystal supersolid state is favored at $N = 1.3 \times 10^5$ [Fig. 2(b)], in contrast to the three-crystal state that forms at lower particle numbers, such as $N = 10^5$ [Fig. 2(b)]. As we will see later, the position of the droplet crystals significantly influences the sharpness of the SF-SSS phase transition.

Next, we determine the ground-state phase diagram, considering different atom numbers N and scattering lengths a for a fixed $a_{dd} = -65.5a_0$. To differentiate between distinct emergent phases, we introduce a contrast measure defined

---

[1]We remark that these multilayered structures are dynamically stable configurations, as has been successfully confirmed through real-time propagation.
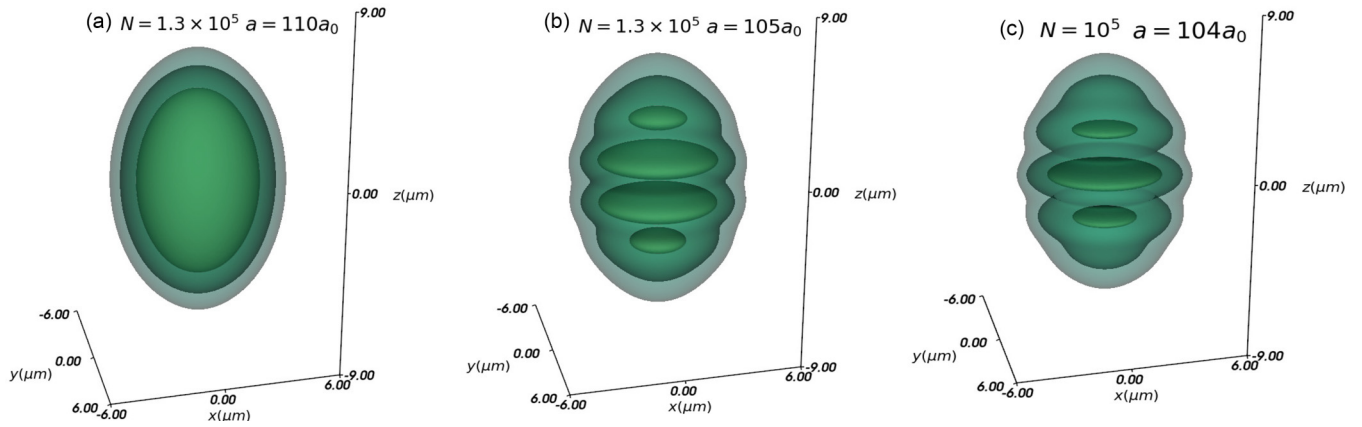
FIG. 2. Density isosurfaces representing (a) the regular superfluid and (b, c) the supersolid state formed by layers of four (b) and three (c) disks for a few selected particle numbers N and scattering lengths a (see the legends). The density isosurfaces are taken at 50, 16, and 2.5% of the maximum density. The system is confined in a harmonic trapping potential with frequencies $(\omega_x, \omega_y, \omega_z)/(2\pi) = (100, 100, 50)$, and dipolar length $a_{dd} = -65.5a_0$. Units of the quantities are indicated within parentheses in the axis labels.

as [6,84]

$$\mathcal{C} = \frac{n_{\max} - n_{\min}}{n_{\max} + n_{\min}}, \qquad (6)$$

where $n_{\max}$ and $n_{\min}$ are the neighboring maximum and minimum densities, respectively. Indeed, we can distinguish between different phases by identifying their characteristic density profiles, particularly through the emergence of modulation in density across the phase transition. It should be noted that the system always possesses an overall parabolic density profile dictated by the harmonic confinement and, hence, we refer to the *periodic density modulation* as an order parameter of the system. The periodic density modulation is absent in the SF phase, resulting in $\mathcal{C} = 0$. However, it is a distinctive characteristic feature of both the SSS and SD phases. The SSS and SD phases can be distinguished from each other by the values of the local minima in the density. In the SD phase, they become zero, and the modulated density structures are completely isolated, resulting in a density contrast of $\mathcal{C} = 1$. Conversely, in the SSS phase, the localized structures are connected via dilute background densities, resulting in $0 < \mathcal{C} < 1$. The thick blue line in Fig. 3 indicates the transition from a regular SF to SSS. Notably, the critical scattering length at which the transition occurs increases with the particle number N. Additionally, the number and positions of disks are sensitive to N (and hence density). When a crystal develops at $z = 0$ and the remaining crystals appear symmetrically in pairs on both sides, an odd number of crystals form. Conversely, if there is a density dip at $z = 0$, only an even number of crystals can be formed. These distinct arrangements often correspond to closely positioned local-energy minima. To accurately determine the minimum-energy state and identify the crystal state with an even or odd number, we have employed different initial guesses; see the Appendix B for details. For instance, an even number of disk-shaped droplet arrays can form along the z direction (see the triangular markers) for particle numbers between $1.03 \times 10^5 < N < 1.04 \times 10^5$. However, for a lower number of particles, an odd number of droplets (see the circular markers) become energetically favorable. The increasing number of odd and even droplet

crystals can be identified with the growing particle number in a similar manner. At fixed particle number, further decreasing a results in the gradual suppression of the density between individual disks, ultimately rendering them completely isolated from each other. The onset of the SD phase is indicated in Fig. 3 by the thin red line. This transition also manifests by a density maximum (circular markers) or minimum (triangular markers) at $z = 0$, depending on particle number. The SSS-SD phase transition exhibits a highly continuous nature (see also Fig. 4) and thus, for the sake of convenience in the numerical simulation, it is necessary to limit the contrast to a value close to unity in order to identify the SSS-SD phase transition. The specific scattering length at which this transition occurs is identified when $\mathcal{C} > 0.99$ [91]. In our current setup, we notice that an odd number of disks with one situated at the center form for particle numbers between $9 \times 10^4 < N < 9.1 \times 10^4$. Typical examples for isolated three- and four-disk stacks are demonstrated for $N = 7 \times 10^4$ and 10^5 particles, respectively, in Figs. 3(b) and 3(c), showing integrated density profiles defined as $n_{1D}(z) = \int dx dy |\psi(x, y, z)|^2$. This observable, which we also utilize later, is experimentally detectable, e.g., via *in situ* imaging [5,13].

To gain a deeper understanding of the nature of the transition, we investigate the contrast $\mathcal{C}$ as a function of the scattering length a for two different particle numbers; see Fig. 4. In addition, we use Leggett's upper bound to estimate the superfluid fraction f_s [18,106] in the central region of length $2L$:[2]

$$f_s = \frac{(2L)^2}{N} \left[\int dz \frac{1}{\int dx dy |\psi|^2} \right]^{-1}. \qquad (7)$$

For $N = 1.3 \times 10^5$ particles, we observe the continuous formation of disks on both sides of $z = 0$ as $\mathcal{C}(f_s)$ gradually approaches zero (one), indicating the formation of modulated

---

[2]The length $2L$ spans the central region between the first two side minima for three disks and the first two side maxima for four disks, along the z axis [83].
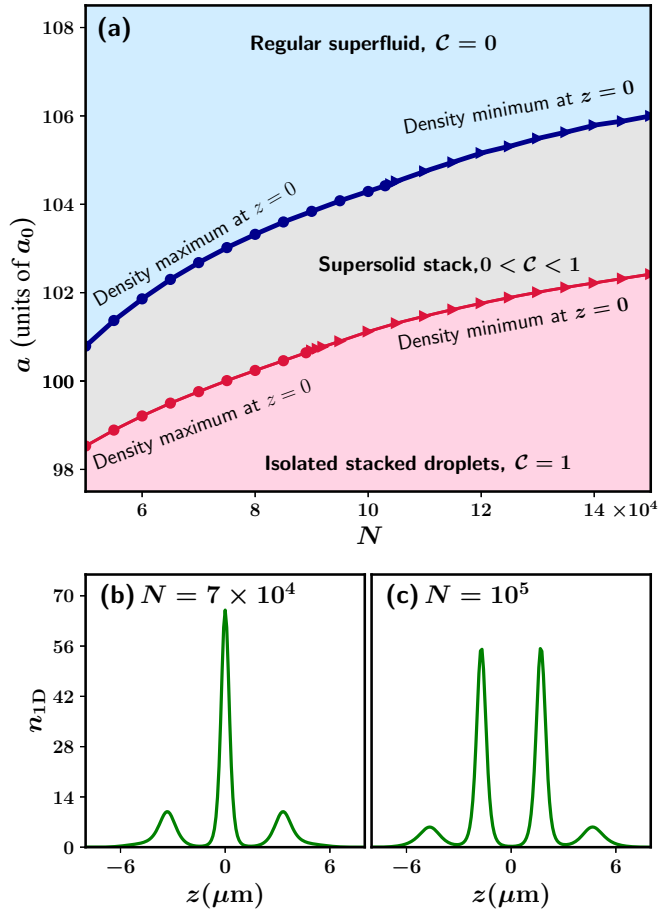
FIG. 3. (a) Phase diagram of the antidipolar condensate in terms of the particle number N and scattering length a. The thick blue line separates the supersolid disk phases (light gray) from the unmodulated superfluid phase (light blue), which occurs when the contrast $\mathcal{C} = 0$. On the other hand, the thin red line divides the supersolid disks from isolated disks (light pink) where the contrast is $\mathcal{C} = 1$. The triangular markers indicate a phase transition that manifests via a density minimum near the center of the trap, while the circular markers denote the same via a density maximum. The bottom panels show the integrated density profiles n_{1D}, in units of 1000 μm^{-1} along the z direction for (b) $N = 7 \times 10^4$ and (c) $N = 10^5$. All other parameters are the same as in Fig. 2. Units of the quantities are indicated within parentheses in the axis labels.

density structures with a strong superfluid connection between them. As the scattering length a decreases, we observe that $\mathcal{C}(f_s)$ increases (decreases) due to a pronounced density modulation. At $a = 102.1a_0$, the disks become completely isolated from each other and $\mathcal{C} > 0.99$. Interestingly, for $N = 10^5$ particles, the superfluid to supersolid transition is much sharper, but it still remains continuous. We observe a disk formation at $z = 0$ for this transition, unlike in the case of $N = 1.3 \times 10^5$ particles. The contrast drops from $\mathcal{C} = 0.252$ at $a = 104.24a_0$ to $\mathcal{C} = 0$ at $a = 104.27a_0$. Our results are consistent with the findings of Ref. [60], where the supersolid phase transition is argued to be continuous (i.e., second-order phase transition) at larger particle numbers closer to the thermodynamic limit due to insignificant kinetic-energy contributions. A close inspection also reveals that the superfluid state just before the
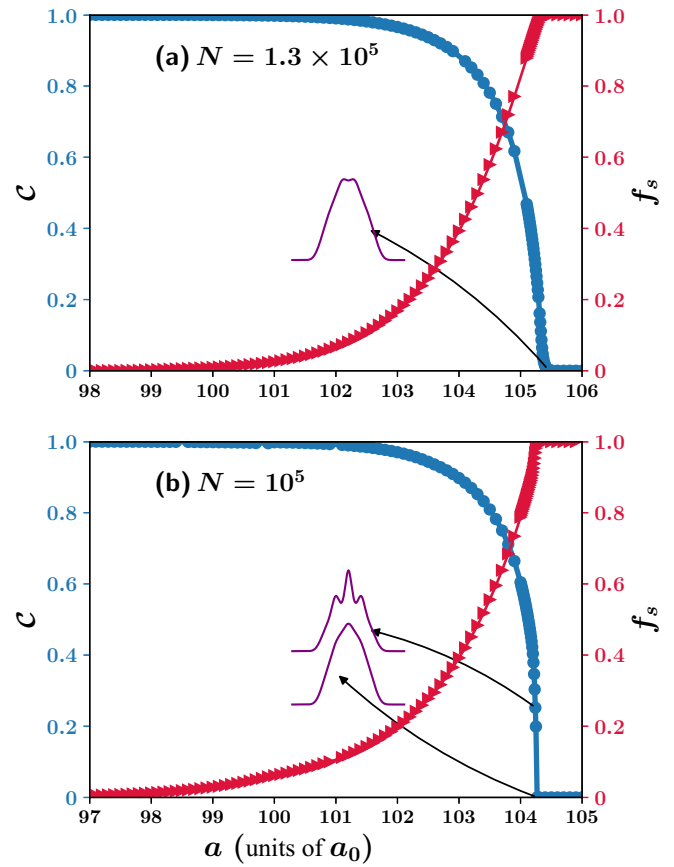

FIG. 4. Ground-state contrast $\mathcal{C}$ (blue circular markers) and superfluid fraction f_s (red triangular markers) as a function of the scattering length a for two different particle numbers (a) $N = 1.3 \times 10^5$ and (b) $N = 10^5$. The insets show the integrated density profiles close to the supersolid and superfluid transitions at scattering length $a = 105.45a_0$ for $N = 1.3 \times 10^5$ (a), and $a = 104.24a_0$ and $104.27a_0$ for $N = 10^5$ (b). All other parameters are the same as in Fig. 2. Units of the quantities are indicated within parentheses in the axis labels.

transition to the supersolid state does not exhibit the typical parabolic density. Nonetheless, they are still classified as superfluid since they demonstrate a nonperiodic density modulation. For instance, for $N = 1.3 \times 10^5$, n_{1D} has a tendency to develop a flat top (Fig. 4) profile, while for $N = 10^5$ a sharp peak appears [Fig. 4(b)]. Turning to the SD side of the curves, we observe that the contrast C gradually approaches unity as the system enters the isolated droplet regime for both $N = 1.3 \times 10^5$ and 10^5 particles. This substantiates also the very continuous nature of the SSS-SD phase transition. Notably, our numerical simulations show that the superfluid fraction, as calculated by Eq. (7), does not completely vanish during the SSS-SD transition. Additionally, f_s gradually decreases and becomes $f_s < 0.1$ when $\mathcal{C} > 0.99$, indicating the transition to the SD phase. Let us emphasize that both f_s and $\mathcal{C}$ accurately predict the transition from the SF to SSS phase as their respective values deviate from unity. However, for the SSS-SD phase transition, we find that $\mathcal{C}$ serves as a better indicator of the isolation of the localized droplets from each other, as f_s still has a finite value when $\mathcal{C}$ reaches close to
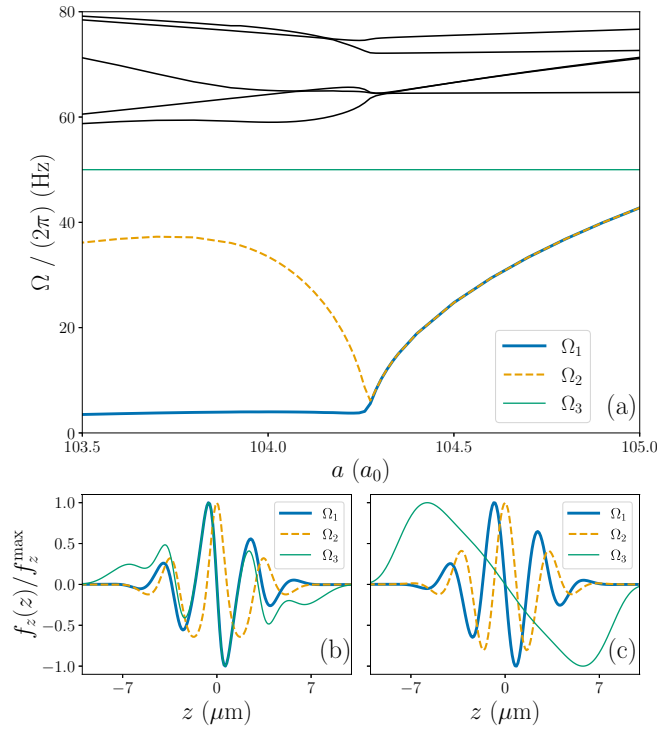
FIG. 5. (a) Frequencies $\Omega/(2\pi)$ of the eight lowest excitation modes as a function of the scattering length a. The two lower panels show the function $f_z(z) = \int dx dy f(\mathbf{r})$ for the three lowest modes (Ω_1, Ω_2, and Ω_3) in the (b) supersolid phase for $a = 104a_0$ and in the (c) superfluid phase for $a = 104.7a_0$, normalized to the maximal value f_z^{max}. The system consists of $N = 10^5$ particles, and all other parameters are the same as in Fig. 2. Units of the quantities are indicated within parentheses in the axis labels.

unity ($\mathcal{C} > 0.99$). It is evident that Leggett's upper bound can eventually approach zero deep into the SD regime. For example, it becomes $f_s < 5 \times 10^{-3}$ at $97a_0$ for $N = 10^5$, but at $a = 98.5a_0$ for $N = 1.3 \times 10^5$ (see Fig. 4). This observation is consistent with the findings of Ref. [91].

B. Collective excitation spectra

Having identified the ground-state phase diagram and showcased some density profiles, we turn to study the behavior of the collective excitations. The low-lying collective excitation spectra for the supersolid phase in the regular dipolar condensate have been reported in Refs. [9,12,13,37,39,107,108]. To accomplish this for the antidipolar condensate, we fix the particle number at $N = 10^5$ and compute the spectrum over a range of values of the s-wave scattering length by solving the BdG Eq. (3). The obtained results are displayed in Fig. 5. Specifically, we have examined the low-lying excitations that are primarily related to excitations in the z direction. The frequencies of the eight lowest modes are presented in Fig. 5(a), and we will primarily focus on the three-lowest modes, denoted by Ω_1, Ω_2, and Ω_3, respectively. In the SF regime the two lowest modes (Ω_1, Ω_2) are degenerate, namely, $\Omega_1 = \Omega_2$. We notice that as the scattering length is decreased from $a = 105a_0$, the two degenerate modes eventually split into two around $a \approx 104.26a_0$,

marking the transition from the superfluid to the supersolid phase. It is interesting to note that the point at which the degeneracy breaks coincides with the point where the contrast drops to zero, as shown in Fig. 4(b). This implies that the breaking of degeneracy can be used as a precise definition of the transition point from the superfluid to the supersolid phase. This behavior is analogous to what has been observed for a regular dipolar supersolid in an elongated harmonic trap [12]. To investigate the nature of these modes further, we note that to the lowest nonvanishing order in ε, the density can be written as

$$n(\mathbf{r}, t) = \psi_0^2(\mathbf{r}) + 2\sqrt{2}\varepsilon f(\mathbf{r})\psi_0(\mathbf{r})\cos(\Omega t). \qquad (8)$$

The time evolution of the density associated with a mode is consequently characterized by the function f, and we display the integrated version $f_z(z) = \int dx dy f(\mathbf{r})$ of the three lowest modes in Figs. 5(b) and 5(c). Note that the $f_z(z)$ characterizes how the density varies along the weakly confined direction (z axis) and thus provides information about the spatial distribution and nature of the collective excitations. The modes in the SSS phase at $a = 104a_0$ are shown in Fig. 5(b), while the modes in the superfluid phase at $a = 104.7a_0$ are shown in Fig. 5(c). Interestingly, the two lowest modes are very similar in both phases, although their effects are quite different due to their different spatial distributions. For the supersolid, the lowest mode Ω_1 corresponds to a center-of-mass excitation where the high-density regions move back and forth but out of phase with the background supersolid. Thus it is a Nambu-Goldstone mode (called the out-of-phase Goldstone mode [11]) associated with the spontaneous breaking of translation symmetry [109]. The second-lowest mode is a Higgs (amplitude) mode [110], where the crystalline regions periodically increase and decrease in density in a fashion opposite to that of the superfluid background, and thus corresponds to a compressional mode. As we will see in the following, such compressional modes get activated during the generation of the supersolid state via an interaction quench. The third-lowest mode Ω_3 is the dipole mode, which has a constant frequency $\Omega/(2\pi) = 50$ Hz independent of the interaction strength [111] and remains decoupled from other modes, thereby serving as a gauge for numerical accuracy. It features an overall center-of-mass motion of the system at the trap frequency. In the superfluid phase [Fig. 5(c)], the first two modes, Ω_1 and Ω_2, have the same frequency, $\Omega_1 = \Omega_2$, and the third mode Ω_3 is the dipole mode. The Ω_3 changes character significantly as the system transitions from a superfluid to a supersolid. The corresponding function f_z of Ω_3 in the supersolid phase has a very prominent dipolelike structure that is composed of a single positive and negative region; see the thin solid green curve in Fig. 5(c). This mode in the supersolid phase [the thin solid green line, Ω_3, in Fig. 5(b)] acquires a behavior that appears to be a mix of its lowest mode [the thick solid blue line, Ω_1, in Fig. 5(b)] and the dipole mode in the superfluid phase [Ω_3 in Fig. 5(c)], possessing multiple local minima and maxima. This mode is often attributed to in-phase (between the crystal and the superfluid background) center-of-mass oscillation, referred to as the in-phase Goldstone mode [11].
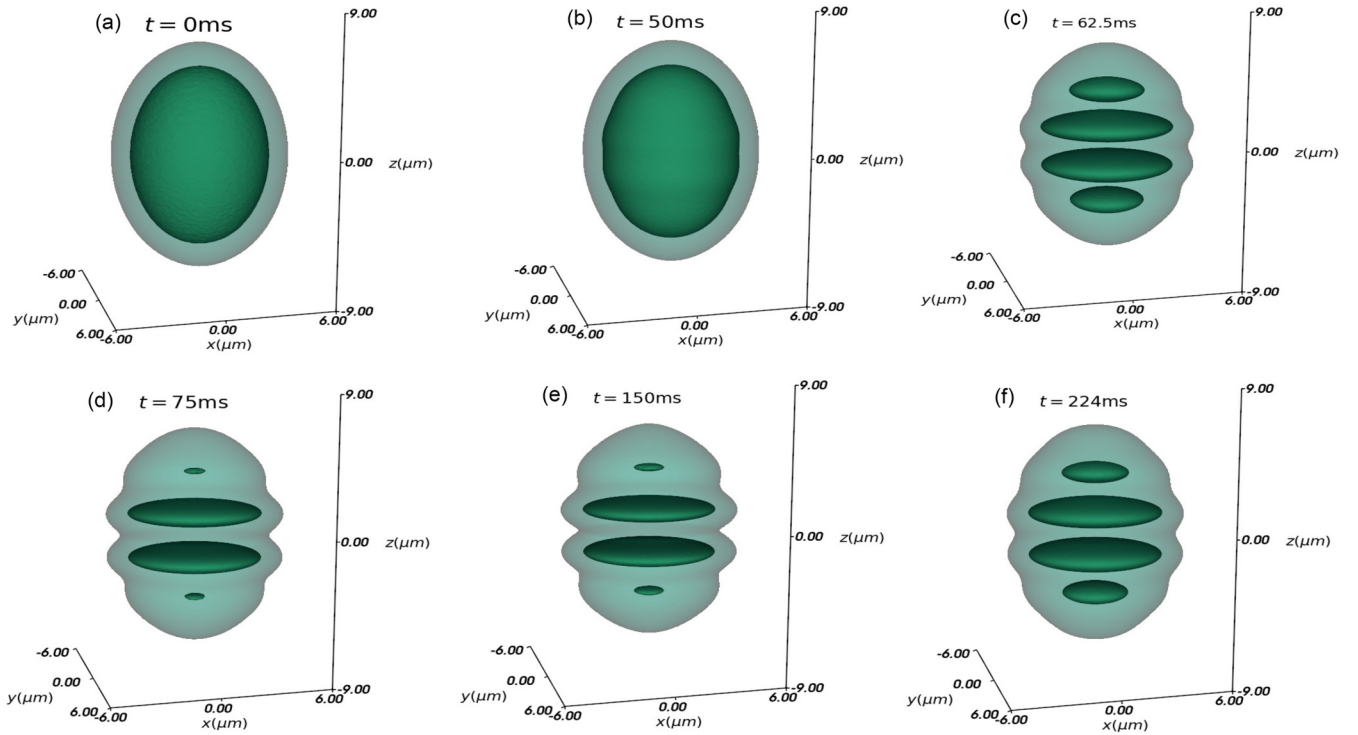
FIG. 6. (a, b) Dynamical generation of supersolid states consisting of stacks of four disks via an interaction quench. The interaction quench has been performed by linearly reducing the scattering length from $a = 110a_0$ to $105a_0$ in $15/\omega_z \approx 47.75$ ms. The density isosurfaces, taken at 20 and 1.5% of the maximum densities, are shown at different instants of time (see the legends). The system is composed of $N = 1.3 \times 10^5$ particles with dipolar length $a_{dd} = -65.5a_0$ and is confined in a potential with frequencies $(\omega_x, \omega_y, \omega_z)/(2\pi) = (100, 100, 50)$ Hz.

IV. QUENCH DYNAMICS ACROSS THE PHASE TRANSITION

After providing evidence of a supersolid state and its underlying collective excitation spectrum within the ground-state phase diagram, we now shift our focus to studying the nonequilibrium dynamics of our system. To trigger these dynamics, we will vary the scattering length from an initial value of $a = a_i$ to a final value of $a = a_f$. A particular focus will be on examining how the layers of disks can be generated dynamically, and such interaction quench is also a well-established protocol in experiments [6,7,41] to generate a supersolid state from an initially unmodulated state. We will also illustrate the emergence of excitations that manifest as density oscillations and how the excitation frequencies relate to those calculated via the BdG analysis at $a = a_f$.

A. Dynamical generation of supersolid disks

We present our results for a system composed of $N = 1.3 \times 10^5$ particles by showing the 3D density isosurfaces in Figs. 6(a)–6(f). Our investigation begins with an initial state prepared at $a_i = 110a_0$. We then introduce a very small amplitude noise [Fig. 6(a)] to the ground state, followed by a gradual decrease of the scattering length to $a_f = 105a_0$ over a time span of 47.75 ms.[3] As the system dynamically enters the SSS phase within the ground-state phase diagram

[Fig. 3(a)], a modulational instability sets in, resulting in the onset of density modulation. This can be observed by careful inspection in Fig. 6(b). Subsequently, for $t > 47.75$ ms, the system quickly forms four prominent circular disks arranged in layers, connected by a dilute superfluid background as depicted in Fig. 6(c). A more precise analysis of the temporally resolved dynamics leading to the SSS phase can be done by invoking the integrated density $n_{1D}(z, t)$. The time evolution of n_{1D} for two different particle numbers is shown in Fig. 7. Indeed, the formation of four disks, with the central two having the highest densities from an initial nonmodulated state, is evident in Fig. 7(a), corresponding to $N = 1.3 \times 10^5$ particles. Similarly, an odd number of disks can be formed dynamically. An example of the formation of a state with three disks is illustrated in Fig. 7(b) for $N = 7 \times 10^4$. The final scattering length $a_f = 102a_0$ is achieved from an initial $a_i = 110a_0$ in the same time span of 47.75 ms as before. The superfluid connection remains more robust for $N = 1.3 \times 10^5$ particles when compared to $N = 7 \times 10^4$. We remark that the value of contrast at the ground state corresponds to $\mathcal{C} = 0.356$ at $a = 105a_0$ for $N = 1.3 \times 10^5$, and $\mathcal{C} = 0.54$ at $a = 102a_0$ for $N = 7 \times 10^4$, implying a weaker background for the latter, which also becomes evident in the dynamically generated SSS phase [see Figs. 7(a) and 7(b)]. Another important observation from Figs. 6(d)–6(f) is that the thickness of each individual crystal changes during the dynamics, implying particle flow

---

[3]This time span is chosen such that we can adiabatically produce the states which have the same number of droplets as those in the

ground state of the system. A sudden quench would typically produce more droplets than the ground state [6].
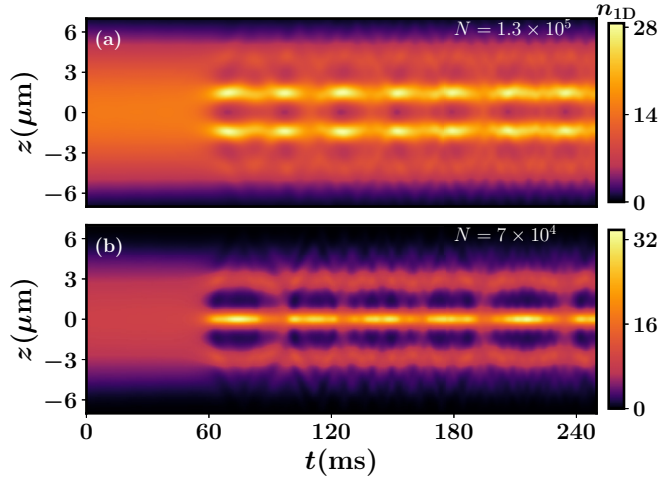
FIG. 7. Generation of supersolid states for two different particle numbers (a) $N = 1.3 \times 10^5$ and (b) $N = 7 \times 10^4$, utilizing the dynamic ramp of the scattering length a from an initial value $a = 110a_0$ to the final value $a = 105a_0$ (a) and $a = 102a_0$ (b). The colorbar represents the integrated density n_{1D} in units of $1000\ \mu m^{-1}$. The duration of the dynamic ramp is $15/\omega_z \approx 47.75$ ms. All other parameters are the same as in Fig. 2.

among them as well as the emergence of density oscillations. This particle flow causes a persistent alteration of the density, radial width, and thickness [see Figs. 7(a)–7(f)], thereby triggering compressional dynamics, which we will expound on next.

B. Collective oscillation during dynamics

Here we evaluate the extent to which the density of the system during the time evolution remains similar to that of the ground state at the same scattering length. This can be monitored by analyzing the observable $\Delta n(t)$, as given by

$$\Delta n(t) = (1/N) \int d\mathbf{r}(|\psi(\mathbf{r}, t)|^2 - |\psi_0(\mathbf{r})|^2), \quad (9)$$

where ψ_0 represents the ground-state wave function at a_f. When the value of $\Delta n(t)$ approaches zero, it indicates that the dynamically generated supersolid state is very similar to the ground state. However, any deviation from zero arises due to the collective excitations triggered during the dynamics. The behavior of $\Delta n(t)$, which relates to the density evolution displayed in Fig. 7(a) and 7(b), has been presented in Fig. 8(a). Note that $\Delta n(t = 0)$ is higher for $N = 7 \times 10^4$ than for $N = 1.3 \times 10^5$ due to a stronger superfluid connection in the final state, ψ_0, of the former, making it much closer to the initial superfluid ground state. As the scattering length is gradually ramped down to the final value, $\Delta n(t)$ gradually decreases and eventually reaches a minimum, as shown in Fig. 8(a). This minimum value indicates the generation of a density-modulated state that closely resembles the ground state at the final scattering length a_f. Subsequently, $\Delta n(t)$ exhibits an oscillatory behavior that involves multiple oscillation frequencies. The oscillation amplitude is larger for $N = 7 \times 10^4$ than $N = 1.3 \times 10^5$ because the change in scattering length
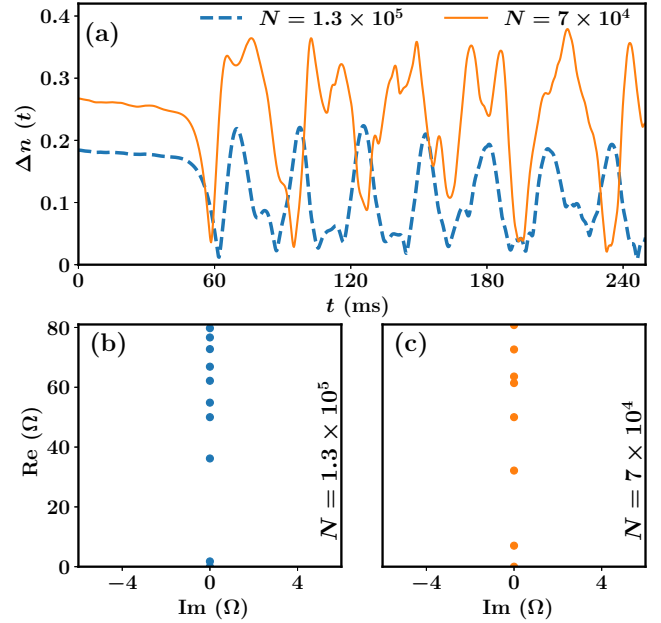

FIG. 8. (a) Time evolution of the integrated density difference with respect to the ground state ψ_0 at the final scattering lengths is quantified via $\Delta n(t) = (1/N) \int d\mathbf{r}(|\psi(\mathbf{r}; t)|^2 - |\psi_0(\mathbf{r})|^2)$ for two different particle numbers (see the legends). The dynamics is triggered by ramping the scattering length from $a = 110a_0$ to $105a_0$ ($N = 1.3 \times 10^5$), and $a = 102a_0$ ($N = 7 \times 10^4$). The real and imaginary parts of the collective excitation spectra Ω are presented in (b) for $N = 1.3 \times 10^5$ and (c) for $N = 7 \times 10^4$, calculated by BdG analysis at $a = 105a_0$ and $102a_0$, respectively. The BdG frequencies are shown in units of $2\pi \times$ Hz.

$a_f - a_i$ is larger in the same time span, making the quench less adiabatic in the former case.

As mentioned earlier, such oscillations in $\Delta n(t)$ stem from the continuous particle flow between the crystal and background, leading to compressional dynamics. The two dominant frequencies of oscillations are calculated by performing a Fourier transformation of $\Delta n(t)$,[4] yielding $\omega_{f_1}/(2\pi) \approx 36 \pm 0.5$ Hz and $\omega_{f_2}/(2\pi) \approx 72 \pm 0.5$ Hz for $N = 1.3 \times 10^5$, and $\omega_{f_1}/(2\pi) \approx 28 \pm 0.5$ Hz and $\omega_{f_2}/(2\pi) \approx 72 \pm 0.5$ Hz for $N = 7 \times 10^4$. Next, we check whether these frequencies are related to the low-lying excitations of the ground state at the final scattering length, a_f. It should be noted that the excitation spectra at scattering lengths other than the final value may also be triggered during the quenching process. However, their contribution to the oscillation of $\Delta n(t)$ is expected to be negligible, as the system spends most of the time at a_f. The frequencies of the low-lying collective excitation spectra calculated at $a = 105a_0$ and $102a_0$ are presented in Figs. 8(b) and 8(c) for $N = 1.3 \times 10^5$ and 7×10^4, respectively. Notably, the dominant oscillation frequency in $\Delta n(t)$ is very close to the second frequency (excluding the zero frequency) that corresponds to the Higgs amplitude mode, as depicted in Figs. 8(b)

---

[4]To compute the frequencies, we have propagated $\Delta n(t)$ until the time $T_f = 1's$, and as a result the maximum frequency error is estimated to be $1/T_f = 1$ Hz.
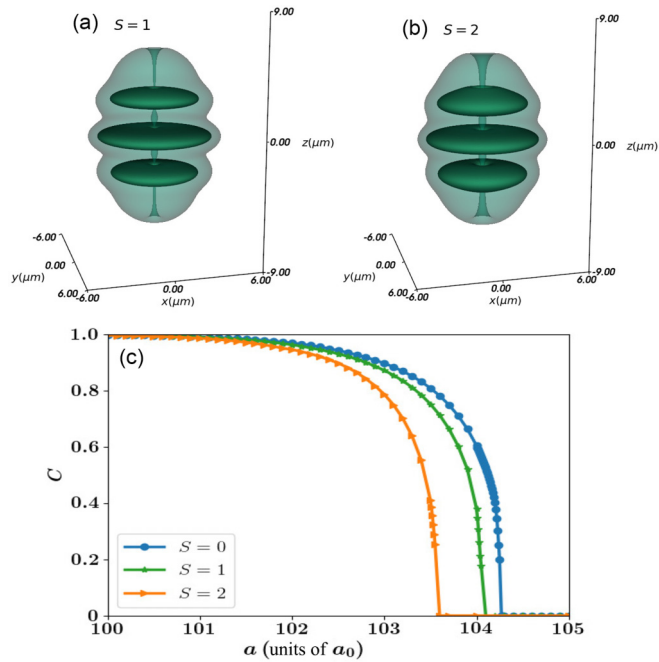
FIG. 9. Density isosurfaces within a supersolid state in the presence of a vortex line with charge (a) $S = 1$ and (b) $S = 2$. (c) The contrast $\mathcal{C}$ as a function of scattering length a in the presence ($S = 1, S = 2$) or absence ($S = 0$) of a vortex line. The density isosurfaces represent 20 and 2.5% of the maximum density. The ^{164}Dy system is composed of $N = 10^5$ particles with dipolar length $a_{dd} = -65.5a_0$, and confined in a trapping potential with frequencies $(\omega_x, \omega_y, \omega_z)/(2\pi) = (100, 100, 50)$ Hz. Units of the quantities are indicated within parentheses in the axis labels.

and 8(c). Additionally, the second dominant frequency close to 72 Hz is also evident in the spectrum. Finally, it should be noted that we have illustrated the intricate connection discussed above by considering these two particle numbers as representative of three- and four-crystal states. However, the discussion is generally valid for all states in the SSS phase, where the nonequilibrium dynamics induced by the quench indeed emanates from triggering the low-lying excitations of the system.

V. IMPACT OF A VORTEX LINE

Let us finally briefly illustrate the effect of a nonlinear defect on the formation of multiple-disk structures and the associated superfluid background. As the disks are relatively flat structures, they offer an opportunity to investigate quasi-two-dimensional (2D) physics, particularly in relation to vortices. Hence, it is crucial to examine the influence of vortex line penetration on the phase transition. To realize a vortex line of charge S passing through the center of the disks, we perform the transformation

$$\psi(x, y, z) = \psi(x, y, z)e^{iS \tan^{-1}(y/x)} \quad (10)$$

to the wave function during the imaginary time evolution, which ensures a vanishing density at the center.

Figures 9(a) and 9(b) depict the 3D isosurfaces representing the supersolid state for $S = 1$ and 2, respectively, realized

at $a = 103a_0$ for $N = 10^5$ particles. The vortex line has a larger radial thickness in the dilute superfluid background than in the localized crystal structure, which varies between $S = 1$ and 2. This suggests that the superfluid connection between the crystal changes due to the presence of a vortex. To investigate this further, we explore whether imprinting a vortex line changes the supersolid region, as shown in Fig. 9. The contrast $\mathcal{C}$ is plotted as a function of the scattering length a in both the presence and absence of a vortex line. The results show that a higher-charge vortex shifts the supersolid phase towards a lower scattering length compared to the vortex-free system. However, the contrasts asymptotically approach each other towards the isolated droplet phases, indicating that the SSS to SD transition is not affected by the presence of a vortex. Between the SF and SSS phase, the contrast decreases sharply towards lower values for higher vortex charges. It is energetically costly for a vortex to dig a hole within the highly localized crystal compared to the dilute superfluid, and therefore it increases superfluid connection, minimizing the crystal density.

In addition, we remark that we have analyzed the stability of vortex lines in real-time dynamics. It is observed that a single charge vortex remains stable, but the double-unit charged vortex line eventually bends and breaks. However, the detailed discussion of their dynamics is beyond the scope of this paper.

VI. CONCLUSIONS

In this paper, we have reported a supersolid state formed in the form of stacked disklike droplets connected by a dilute superfluid in an antidipolar condensate [90]. Considering an elongated geometry with experimentally relevant trapping frequencies we have presented a phase diagram in the parameter space of particle number N and scattering length a, identifying the regions of existence for a superfluid, supersolid disks, and isolated disks.

We have utilized a contrast measure and superfluid fraction to differentiate between different emergent phases. As the scattering length decreases, the contrast (superfluid fraction) increases (decreases) due to a pronounced density modulation, leading to the formation of disk-shaped density modulations. The critical scattering length for the transition from a regular superfluid to a supersolid stack phase increases with the particle number. The number and distribution of disks along the z direction are strongly dependent on the total number of particles.

Building upon the phase diagram, we have studied the collective excitation spectrum across the superfluid-supersolid phase transition in the antidipolar condensate. Specifically, we have computed the frequency of the eight lowest modes and characterized the density of the first three modes. The breaking of degeneracy of the two lowest-lying modes marks the transition point from the superfluid to the supersolid stack phase. Additionally, the third lowest mode, the so-called dipole mode, also changes significantly as the system undergoes a phase transition. We have also examined the influence of vortex line penetration on the phase transition, with the supersolid region shifting towards weaker contact interaction upon imprinting a vortex line.

As a next step, we have studied the nonequilibrium dynamics triggered by ramping down the scattering length across the superfluid and supersolid phase transition. We have demonstrated the dynamic generation of four and three disks connected by a dilute superfluid, considering two different particle numbers. The particle flow between the disks triggers a collective oscillation in the density. We have identified two dominant frequencies of oscillations, which can also be found in the low-lying collective excitation spectra of the ground state at the final scattering length.

The present paper has the potential to pave the way for numerous promising research directions for future endeavors. To further enhance our understanding, it would be fascinating to investigate the response of the disks and background superfluid to external rotation and dynamically observe how vortex lines penetrate through the disklike density modulations. Currently, vortices are being sought actively in dipolar supersolids, and the recent creation of vortices in an unmodulated dipolar condensate presents optimistic prospects in this area [112,113]. The 2D nature of the crystal makes the antidipolar condensate an intriguing setup along that direction. Further exploration will be undertaken to examine supersolid stacks and isolated stacked droplets in the context of binary mixtures [114]. Direct formation of such a supersolid structure via evaporative cooling along the line of Ref. [41] and investigating the thermal properties [115] would be highly interesting.

APPENDIX A: THREE-BODY ATOM LOSS

In experiments, the lifetime of the supersolid state is limited by three-body losses, which has been previously discussed in the context of dBECs with positive dipolar lengths [6–8]. This type of losses is caused by highly localized density arrays, making it crucial to understand how it affects the formation and persistence of the SSS in anti-dBECs. A comprehensive understanding of this phenomenon is necessary for the successful experimental realization of SSS states. In simulations, the loss can be modeled by adding an imaginary contribution, represented by $(-i\hbar K_3/2)|\psi(\mathbf{r})|^4$, to Eq. (2), where K_3 denotes the three-body recombination rate.

To demonstrate our findings, we examine the formation of a supersolid state in a system composed of $N = 70\,000$ ^{164}Dy atoms by reducing the scattering length from $a = 110a_0$ to $102a_0$ over a period of 47.78 ms. Realistic three-body losses are considered in simulations using the experimentally measured loss coefficient, $K_3 = 1.5 \times 10^{-40}$ m^6/s [6]. Figure 10(a) shows the time evolution of the integrated density $n_{1D}(z)$. The maximum atom loss is $\approx 5.6\%$ of the initial population in 250 ms, as displayed by the blue line in Fig. 10(b). After $t > 47.75$ ms, the initially unmodulated
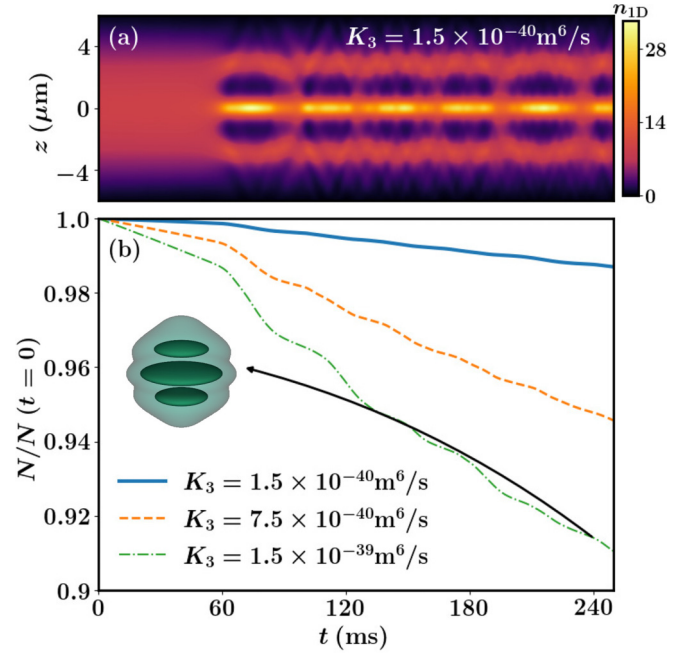

FIG. 10. (a) The time evolution of the integrated density n_{1D} for a quench from an unmodulated state to a supersolid state, including three-body atom loss with a three-body coefficient $K_3 = 1.5 \times 10^{-40}$ m^6/s. The quench has been performed by ramping off the scattering length from $a = 110a_0$ to $102a_0$ in 48 ms. (b) The time evolution of the atom number N for different loss coefficients (see the legends), considering the same quench protocol. The system consists of $N = 70\,000$ ^{164}Dy atoms confined in a harmonic trapping potential with frequencies $(\omega_x, \omega_y, \omega_z)/(2\pi) = (100, 100, 50)$ Hz, with $a_{dd} = -65.5a_0$. The colorbar represents the density in units of 1000 μm^{-1}.

state deforms into three disks. Despite continuous population loss [see Fig. 10(b)], a dilute background density always connects the disks throughout the dynamics. We have also investigated the population loss and supersolid state generation with larger three-body loss coefficients, $K_3 = 7.5 \times 10^{-40}$ and 1.5×10^{-39} m^6/s, respectively. As expected, larger K_3 leads to more atom losses, and $N(t)$ exhibits oscillatory behavior [Fig. 10(b)]. This tendency is caused by the atom losses being influenced by the severe changes in density distribution (via the term $|\psi(\mathbf{r})|^4$), which also undergoes periodic expansion and contraction after the quench. Nonetheless, the supersolid state remains robust in long-time dynamics even for $K_3 = 1.5 \times 10^{-39}$ m^6/s, as evidenced, for example, by the density isosurface at time $t = 240$ ms.

APPENDIX B: COMPUTATIONAL DETAILS

Here, we provide a detailed account of the numerical simulations used to obtain the results described in the main text. The extended Gross-Pitaevskii equation, Eq. (2), is cast into a dimensionless form in our simulations by rescaling the length, the time in terms of the harmonic oscillator length scale $l_{osc} = \sqrt{\hbar/m\omega_z} = 1.11$ μm, and the trap frequency ω_z, respectively. Then the wave function is scaled accordingly as $\psi(\mathbf{r}', t) = \sqrt{l_{osc}^3/N}\psi(\mathbf{r}, t)$. We solve the resulting dimen-

sionless equation using the split-step Crank-Nicolson method; see Ref. [102]. The stationary (lowest-energy) states of the dBEC are obtained through imaginary time propagation. Furthermore, we apply the transformation $\frac{\psi(\mathbf{r},t)}{\|\psi(\mathbf{r},t)\|} \to 1$ at each imaginary time step of this procedure. This preserves the normalization of the wave function, while convergence is reached until relative deviations of the wave function (at every grid point) and energy between consecutive time steps are smaller than 10^{-5} and 10^{-7}, respectively. This solution is then used as an initial state for the dynamical simulations, where the eGP equation is propagated in real time. It should be noted that calculating the stationary state solution of Eq. (2) is an involved task due to many close-lying local minima in the energy surface, which necessitates extensive sampling over many different initial conditions to identify the most probable lowest-energy solutions. Our simulations are carried out in a 3D box characterized by a grid $n_x \times n_y \times n_z$ corresponding to $(128 \times 128 \times 256)$. The employed spatial discretization (grid spacing) refers to $\Delta_x = 0.12 l_{\mathrm{osc}}$, $\Delta_y = 0.12 l_{\mathrm{osc}}$, and $\Delta_z = 0.08 l_{\mathrm{osc}}$, while the time step of the numerical integration is $\Delta_t = 10^{-5}/\omega_z$.

Let us remark that systems involving long-range interactions possess highly nonconvex energy landscapes. Therefore, regardless of the numerical methods employed, simulations tend to converge to different local minima depending on the initial guess. As a result, it is imperative to use different initial guess wave functions and examine which converged state produces the lowest-energy state, corresponding to the ground state of the system.

In our system, we observe droplet-shaped droplets formation along the weakly confined z direction, indicating its one-dimensional nature. Consequently, the remaining task is to accurately determine the distribution of crystals with respect to $z = 0$, which corresponds to the lowest-energy state. To accomplish this, we have employed two different guesses: $\psi_{\sin} = \mathcal{A}_{\sin} e^{-\omega_z^2(\kappa^2 x^2 + \lambda^2 y^2 + z^2)/2} \sin^2(kz)$ and $\psi_{\cos} = \mathcal{A}_{\cos} e^{-\omega_z^2(\kappa^2 x^2 + \lambda^2 y^2 + z^2)/2} \cos^2(kz)$, where $\kappa = \omega_x/\omega_z$ and $\lambda = \omega_y/\omega_z$. The prefactors $\mathcal{A}_j$, with $j \in [\sin, \cos]$, represent the normalization constants. The $\psi_{\sin}$ guess produces a density minimum at $z = 0$ in the converged state, resulting in an even number of droplets, while the $\psi_{\cos}$ guess creates an odd number of droplets. We have also varied the value of k, the distance between the droplet arrays, and found that the converged solution is insensitive to its value for both $\psi_{\sin}$ and $\psi_{\cos}$. In the phase diagram, for each particle number N, we have utilized the aforementioned guesses to determine which one yields the lower energy, thus identifying whether an odd or even number of crystals can form in the ground state.

[1] M. Baranov, Phys. Rep. **464**, 71 (2008).

[2] T. Lahaye, C. Menotti, L. Santos, M. Lewenstein, and T. Pfau, Rep. Prog. Phys. **72**, 126401 (2009).

[3] M. A. Baranov, M. Dalmonte, G. Pupillo, and P. Zoller, Chem. Rev. **112**, 5012 (2012).

[4] F. Böttcher, J.-N. Schmidt, J. Hertkorn, K. S. H. Ng, S. D. Graham, M. Guo, T. Langen, and T. Pfau, Rep. Prog. Phys. **84**, 012403 (2021).

[5] L. Chomaz, I. Ferrier-Barbut, F. Ferlaino, B. Laburthe-Tolra, B. L. Lev, and T. Pfau, Rep. Prog. Phys. **86**, 026401 (2023).

[6] F. Böttcher, J.-N. Schmidt, M. Wenzel, J. Hertkorn, M. Guo, T. Langen, and T. Pfau, Phys. Rev. X **9**, 011051 (2019).

[7] L. Tanzi, E. Lucioni, F. Famà, J. Catani, A. Fioretti, C. Gabbanini, R. N. Bisset, L. Santos, and G. Modugno, Phys. Rev. Lett. **122**, 130405 (2019).

[8] L. Chomaz, D. Petter, P. Ilzhöfer, G. Natale, A. Trautmann, C. Politi, G. Durastante, R. M. W. van Bijnen, A. Patscheider, M. Sohmen, M. J. Mark, and F. Ferlaino, Phys. Rev. X **9**, 021012 (2019).

[9] G. Natale, R. M. W. van Bijnen, A. Patscheider, D. Petter, M. J. Mark, L. Chomaz, and F. Ferlaino, Phys. Rev. Lett. **123**, 050402 (2019).

[10] L. Tanzi, S. M. Roccuzzo, E. Lucioni, F. Fama, A. Fioretti, C. Gabbanini, G. Modugno, A. Recati, and S. Stringari, Nature (London) **574**, 382 (2019).

[11] M. Guo, F. Böttcher, J. Hertkorn, J.-N. Schmidt, M. Wenzel, H. P. Büchler, T. Langen, and T. Pfau, Nature (London) **574**, 386 (2019).

[12] J. Hertkorn, F. Böttcher, M. Guo, J. N. Schmidt, T. Langen, H. P. Büchler, and T. Pfau, Phys. Rev. Lett. **123**, 193002 (2019).

[13] J. Hertkorn, J.-N. Schmidt, M. Guo, F. Böttcher, K. S. H. Ng, S. D. Graham, P. Uerlings, H. P. Büchler, T. Langen, M. Zwierlein, and T. Pfau, Phys. Rev. Lett. **127**, 155301 (2021).

[14] E. P. Gross, Phys. Rev. **106**, 161 (1957). Ann. Phys. (NY) **4**, 57 (1958).

[15] C. N. Yang, Rev. Mod. Phys. **34**, 694 (1962).

[16] A. Andreev and I. Lifshits, Zh. Eksp. Teor. Fiz. **56**, 2057 (1969).

[17] G. V. Chester, Phys. Rev. A **2**, 256 (1970).

[18] A. J. Leggett, Phys. Rev. Lett. **25**, 1543 (1970).

[19] Y. Pomeau and S. Rica, Phys. Rev. Lett. **72**, 2426 (1994).

[20] M. Boninsegni and N. V. Prokof'ev, Rev. Mod. Phys. **84**, 759 (2012).

[21] E. Kim and M. H. W. Chan, Nature (London) **427**, 225 (2004); Science **305**, 1941 (2004).

[22] S. Balibar, Nature (London) **464**, 176 (2010).

[23] D. Y. Kim and M. H. W. Chan, Phys. Rev. Lett. **109**, 155301 (2012).

[24] M. H. W. Chan, R. B. Hallock, and L. Reatto, J. Low Temp. Phys. **172**, 317 (2013).

[25] N. Henkel, R. Nath, and T. Pohl, Phys. Rev. Lett. **104**, 195302 (2010).

[26] F. Cinti, P. Jain, M. Boninsegni, A. Micheli, P. Zoller, and G. Pupillo, Phys. Rev. Lett. **105**, 135301 (2010).

[27] S. Saccani, S. Moroni, and M. Boninsegni, Phys. Rev. B **83**, 092506 (2011).

[28] J. Léonard, A. Morales, P. Zupancic, T. Donner, and T. Esslinger, Science **358**, 1415 (2017); J. Léonard, A. Morales, P. Zupancic, T. Esslinger, and T. Donner, Nature (London) **543**, 87 (2017).

[29] Y. J. Lin, K. Jiménez-García, and I. B. Spielman, Nature (London) **471**, 83 (2011).

[30] J. R. Li, W. Huang, B. Shteynas, S. Burchesky, F. C. Top, E. Su, J. Lee, A. O. Jamison, and W. Ketterle, Phys. Rev. Lett. **117**, 185301 (2016).

[31] J.-R. Li, J. Lee, W. Huang, S. Burchesky, B. Shteynas, F. C. Top, A. O. Jamison, and W. Ketterle, Nature (London) **543**, 91 (2017).

[32] H. Kadau, M. Schmitt, M. Wenzel, C. Wink, T. Maier, I. Ferrier-Barbut, and T. Pfau, Nature (London) **530**, 194 (2016).

[33] I. Ferrier-Barbut, H. Kadau, M. Schmitt, M. Wenzel, and T. Pfau, Phys. Rev. Lett. **116**, 215301 (2016).

[34] M. Schmitt, M. Wenzel, F. Böttcher, I. Ferrier-Barbut, and T. Pfau, Nature (London) **539**, 259 (2016).

[35] F. Böttcher, M. Wenzel, J.-N. Schmidt, M. Guo, T. Langen, I. Ferrier-Barbut, T. Pfau, R. Bombín, J. Sánchez-Baena, J. Boronat, and F. Mazzanti, Phys. Rev. Res. **1**, 033088 (2019).

[36] L. Chomaz, S. Baier, D. Petter, M. J. Mark, F. Wächtler, L. Santos, and F. Ferlaino, Phys. Rev. X **6**, 041039 (2016).

[37] L. Chomaz, R. M. W. van Bijnen, D. Petter, G. Faraoni, S. Baier, J. H. Becher, M. J. Mark, F. Wächtler, L. Santos, and F. Ferlaino, Nat. Phys. **14**, 442 (2018).

[38] M. Sohmen, C. Politi, L. Klaus, L. Chomaz, M. J. Mark, M. A. Norcia, and F. Ferlaino, Phys. Rev. Lett. **126**, 233401 (2021).

[39] J.-N. Schmidt, J. Hertkorn, M. Guo, F. Böttcher, M. Schmidt, K. S. H. Ng, S. D. Graham, T. Langen, M. Zwierlein, and T. Pfau, Phys. Rev. Lett. **126**, 193002 (2021).

[40] G. Biagioni, N. Antolini, A. Alaña, M. Modugno, A. Fioretti, C. Gabbanini, L. Tanzi, and G. Modugno, Phys. Rev. X **12**, 021019 (2022).

[41] T. Bland, E. Poli, C. Politi, L. Klaus, M. A. Norcia, F. Ferlaino, L. Santos, and R. N. Bisset, Phys. Rev. Lett. **128**, 195302 (2022).

[42] A. R. P. Lima and A. Pelster, Phys. Rev. A **84**, 041604(R) (2011).

[43] F. Wächtler and L. Santos, Phys. Rev. A **93**, 061603(R) (2016). **94**, 043618 (2016).

[44] R. N. Bisset, R. M. Wilson, D. Baillie, and P. B. Blakie, Phys. Rev. A **94**, 033619 (2016).

[45] D. S. Petrov, Phys. Rev. Lett. **115**, 155302 (2015).

[46] D. S. Petrov and G. E. Astrakharchik, Phys. Rev. Lett. **117**, 100401 (2016).

[47] N. B. Jørgensen, G. M. Bruun, and J. J. Arlt, Phys. Rev. Lett. **121**, 173403 (2018).

[48] C. R. Cabrera, L. Tanzi, J. Sanz, B. Naylor, P. Thomas, P. Cheiney, and L. Tarruell, Science **359**, 301 (2018).

[49] G. Semeghini, G. Ferioli, L. Masi, C. Mazzinghi, L. Wolswijk, F. Minardi, M. Modugno, G. Modugno, M. Inguscio, and M. Fattori, Phys. Rev. Lett. **120**, 235301 (2018).

[50] T. G. Skov, M. G. Skou, N. B. Jørgensen, and J. J. Arlt, Phys. Rev. Lett. **126**, 230404 (2021).

[51] R. N. Bisset and P. B. Blakie, Phys. Rev. A **92**, 061603(R) (2015).

[52] K.-T. Xi and H. Saito, Phys. Rev. A **93**, 011604(R) (2016).

[53] P. B. Blakie, Phys. Rev. A **93**, 033644 (2016).

[54] H. Saito, J. Phys. Soc. Jpn. **85**, 053001 (2016).

[55] A. Macia, J. Sánchez-Baena, J. Boronat, and F. Mazzanti, Phys. Rev. Lett. **117**, 205301 (2016).

[56] D. Baillie, R. M. Wilson, and P. B. Blakie, Phys. Rev. Lett. **119**, 255302 (2017).

[57] D. Edler, C. Mishra, F. Wächtler, R. Nath, S. Sinha, and L. Santos, Phys. Rev. Lett. **119**, 050403 (2017).

[58] D. Baillie and P. B. Blakie, Phys. Rev. Lett. **121**, 195301 (2018).

[59] S. M. Roccuzzo and F. Ancilotto, Phys. Rev. A **99**, 041601(R) (2019).

[60] Y.-C. Zhang, F. Maucher, and T. Pohl, Phys. Rev. Lett. **123**, 015301 (2019).

[61] P. B. Blakie, D. Baillie, L. Chomaz, and F. Ferlaino, Phys. Rev. Res. **2**, 043318 (2020).

[62] C. Mishra, L. Santos, and R. Nath, Phys. Rev. Lett. **124**, 073402 (2020).

[63] L. Chomaz, Phys. Rev. A **102**, 023333 (2020).

[64] E. Poli, T. Bland, C. Politi, L. Klaus, M. A. Norcia, F. Ferlaino, R. N. Bisset, and L. Santos, Phys. Rev. A **104**, 063307 (2021).

[65] J. Hertkorn, J.-N. Schmidt, M. Guo, F. Böttcher, K. S. H. Ng, S. D. Graham, P. Uerlings, T. Langen, M. Zwierlein, and T. Pfau, Phys. Rev. Res. **3**, 033125 (2021).

[66] Y.-C. Zhang, T. Pohl, and F. Maucher, Phys. Rev. A **104**, 013310 (2021).

[67] L. E. Young-S. and S. K. Adhikari, Phys. Rev. A **105**, 033311 (2022).

[68] R. Ghosh, C. Mishra, L. Santos, and R. Nath, Phys. Rev. A **106**, 063318 (2022).

[69] A. Gallemí and L. Santos, Phys. Rev. A **106**, 063301 (2022).

[70] M. Schmidt, L. Lassablière, G. Quéméner, and T. Langen, Phys. Rev. Res. **4**, 013235 (2022).

[71] S. Halder, K. Mukherjee, S. I. Mistakidis, S. Das, P. G. Kevrekidis, P. K. Panigrahi, S. Majumder, and H. R. Sadeghpour, Phys. Rev. Res. **4**, 043124 (2022).

[72] M. N. Tengstrand, D. Boholm, R. Sachdeva, J. Bengtsson, and S. M. Reimann, Phys. Rev. A **103**, 013313 (2021).

[73] S. M. Roccuzzo, A. Recati, and S. Stringari, Phys. Rev. A **105**, 023316 (2022).

[74] P. Ilzhöfer, M. Sohmen, G. Durastante, C. Politi, A. Trautmann, G. Natale, G. Morpurgo, T. Giamarchi, L. Chomaz, M. J. Mark, and F. Ferlaino, Nat. Phys. **17**, 356 (2021).

[75] M. A. Norcia, E. Poli, C. Politi, L. Klaus, T. Bland, M. J. Mark, L. Santos, R. N. Bisset, and F. Ferlaino, Phys. Rev. Lett. **129**, 040403 (2022).

[76] K. Mukherjee and S. M. Reimann, Phys. Rev. A **107**, 043319 (2023).

[77] S. M. Roccuzzo, A. Gallemí, A. Recati, and S. Stringari, Phys. Rev. Lett. **124**, 045702 (2020).

[78] A. Gallemí, S. M. Roccuzzo, S. Stringari, and A. Recati, Phys. Rev. A **102**, 023322 (2020).

[79] M. Šindik, A. Recati, S. M. Roccuzzo, L. Santos, and S. Stringari, Phys. Rev. A **106**, L061303 (2022).

[80] J. C. Smith, D. Baillie, and P. B. Blakie, Phys. Rev. Lett. **126**, 025302 (2021).

[81] R. N. Bisset, L. A. P. Ardila, and L. Santos, Phys. Rev. Lett. **126**, 025301 (2021).

[82] S. Li, U. N. Le, and H. Saito, Phys. Rev. A **105**, L061302 (2022).

[83] D. Scheiermann, L. A. P. Ardila, T. Bland, R. N. Bisset, and L. Santos, Phys. Rev. A **107**, L021302 (2023).

[84] T. Bland, E. Poli, L. A. P. Ardila, L. Santos, F. Ferlaino, and R. N. Bisset, Phys. Rev. A **106**, 053322 (2022).

[85] S. Halder, S. Das, and S. Majumder, Phys. Rev. A **107**, 063303 (2023).

[86] Y. Tang, W. Kao, K.-Y. Li, and B. L. Lev, Phys. Rev. Lett. **120**, 230401 (2018).

[87] S. Giovanazzi, A. Görlitz, and T. Pfau, Phys. Rev. Lett. **89**, 130401 (2002).

[88] D. Baillie and P. B. Blakie, Phys. Rev. A **101**, 043606 (2020).

[89] S. B. Prasad, T. Bland, B. C. Mulkerin, N. G. Parker, and A. M. Martin, Phys. Rev. Lett. **122**, 050401 (2019).

[90] M. Wenzel, Macroscopic states of dipolar quantum gases, Ph.D thesis, University of Stuttgart, Germany, 2022.

[91] W. Kirkby, T. Bland, and B. R. N. Ferlaino, arXiv:2301.08007.

[92] T. Bilitewski, G. A. Dominguez-Castro, D. Wellnitz, A. M. Rey, and L. Santos, Phys. Rev. A **108**, 013313 (2023).

[93] G. Natale, T. Bland, S. Gschwendtner, L. Lafforgue, D. S. Grün, A. Patscheider, M. J. Mark, and F. Ferlaino, Commun. Phys. **5**, 227 (2022).

[94] L. Du, P. Barral, M. Cantara, J. de Hond, Y.-K. Lu, and W. Ketterle, arXiv:2302.07209.

[95] R. M. Wilson, S. Ronen, and J. L. Bohn, Phys. Rev. A **79**, 013621 (2009).

[96] R. M. Wilson, S. Ronen, and J. L. Bohn, Phys. Rev. A **80**, 023614 (2009).

[97] H.-Y. Lu, H. Lu, J.-N. Zhang, R.-Z. Qiu, H. Pu, and S. Yi, Phys. Rev. A **82**, 023622 (2010).

[98] P. B. Blakie, D. Baillie, and R. N. Bisset, Phys. Rev. A **86**, 021604(R) (2012).

[99] A. D. Martin and P. B. Blakie, Phys. Rev. A **86**, 053623 (2012).

[100] R. Schützhold, M. Uhlmann, Y. Xu, and U. R. Fischer, Int. J. Mod. Phys. B **20**, 3555 (2006).

[101] A. R. P. Lima and A. Pelster, Phys. Rev. A **86**, 063609 (2012).

[102] J. Crank and P. Nicolson, Math. Proc. Camb. Phil. Soc. **43**, 50 (1947).

[103] X. Antoine, W. Bao, and C. Besse, Comput. Phys. Commun. **184**, 2621 (2013).

[104] C. J. Pethick and H. Smith, *Bose-Einstein Condensation in Dilute Gases* (Cambridge University, Cambridge, England, 2002).

[105] S. Stringari and L. Pitaevskii, *Bose-Einstein Condensation* (Oxford University, New York, 2003).

[106] A. J. Leggett, J. Stat. Phys. **93**, 927 (1998).

[107] J. Hertkorn, J.-N. Schmidt, F. Böttcher, M. Guo, M. Schmidt, K. S. H. Ng, S. D. Graham, H. P. Büchler, T. Langen, M. Zwierlein, and T. Pfau, Phys. Rev. X **11**, 011037 (2021).

[108] C. Bühler, T. Ilg, and H. P. Büchler, arXiv:2211.17251.

[109] Y. Nambu, Rev. Mod. Phys. **81**, 1015 (2009).

[110] D. Pekker and C. Varma, Annu. Rev. Condens. Matter Phys. **6**, 269 (2015).

[111] W. Kohn, Phys. Rev. **123**, 1242 (1961).

[112] L. Klaus, T. Bland, E. Poli, C. Politi, G. Lamporesi, E. Casotti, R. N. Bisset, M. J. Mark, and F. Ferlaino, Nat. Phys. **18**, 1453 (2022).

[113] T. Bland, G. Lamporesi, M. J. Mark, and F. Ferlaino, arXiv:2303.13263.

[114] M. Arazo, A. Gallemí, M. Guilleumas, R. Mayol, and L. Santos, arXiv:2303.02087.

[115] J. Sánchez-Baena, C. Politi, F. Maucher, F. Ferlaino, and T. Pohl, Nat. Commun. **14**, 1868 (2023).